Detection of time variable gravity signals using terrestrial clock networks

Asha Vincent [*], Jürgen Müller

Leibniz University Hannover, Institute of Geodesy, Schneiderberg 50, Hannover 30167, Germany

Abstract

The relativistic redshift between two earth-bound clocks can be interpreted in terms of gravity potential variation between the clock locations. A clock with a fractional frequency uncertainty of 10^{-18} is sensitive to a gravity potential variation of 0.1 m^2/s^2 or a height difference of 1 cm. Case studies for four regions affected by different mass change processes - Himalaya, Amazon, Greenland, and Fennoscandia - have been carried out. As the clocks rest on the deformable Earth's surface, clock observations do not only include potential variations due to mass changes but also associated variations due to the vertical deformation of the land. For the simulations, vertical displacements were derived from real GNSS (Global Navigation Satellite Systems) measurements, and mass variations were computed from GRACE (Gravity Recovery And Climate Experiment) solutions. In the Himalayan region, seasonal variations with a maximum range of $[-0.2 \quad 0.2]$ m^2/s^2 were obtained. There, early and long-lasting precipitation patterns in North-East India and the gradual spreading towards the West can be observed by a dedicated clock network. For the Amazon region, seasonal variations with a maximum range of $[-0.5 \quad 0.5]$ m^2/s^2 observed by clocks also reveals the Amazon's seasonal properties of annual rainfall variability at the North and South of the equator. The rainy season in the North of the equator is during the summer season from June to August, but from November to April in the South of the equator. The long-term trend of the ice mass loss in Greenland between 2004 and 2015 causes signals of potential variations of 1 m^2/s^2 that again can clearly be observed by clock measurements. Especially, the higher rates of mass variations in the west and south parts of Greenland can well be observed. The land uplift pattern of Fennoscandia due to the GIA (Glacial Isostatic Adjustment) can also be detected using optical clocks, however, the vertical deformations dominate the signal and not the mass changes. These examples illustrate that terrestrial clock networks can be used in the future as a modern tool for detecting various time-variable gravity signals for understanding the regional/local patterns of the variations and for providing complementary information to other geodetic techniques.

1. Introduction

Mass is continuously redistributing in our dynamic earth system resulting from precipitation, groundwater changes, ice mass loss, glacial isostatic adjustment, etc. Together with the mass change, there is also a geometrical deformation of the earth's surface associated with the surface load (Love, 1909). Time series of gravity variations reflect change processes in the Earth system and ultimately point to climate change (Tapley et al., 2019). The detection of time-variable gravity signals with high accuracy is a central task of geodesy (Pail et al., 2015).

As introduced by Bjerhammar (1985) the novel method of chronometric geodesy evolved from the general relativity framework (Delva et al., 2019). The frequency change of a clock can be interpreted directly in terms of the gravita-

* Corresponding author.
E-mail addresses: vincent@ife.uni-hannover.de (A. Vincent), mueller@ife.uni-hannover.de (J. Müller).

tional potential change at the clock location if compared to a clock at a stable location (Bjerhammar, 1986). Optical clocks with their fast development in recent years provide a novel geodetic measurement method (Wu et al., 2019). Utilizing the concept of gravitational redshift, optical atomic clocks with fractional frequency uncertainty of 10^{-18} will be able to detect a gravity potential variation of 0.1 m²/s² or a height difference of 1 cm.

2. Time-variable gravity signals

There are many different geophysical processes that result in reshaping the gravity potential (geoid) in the time domain. The Earth's gravity potential contains temporal variations along with the predominant static part (Müller et al., 2018). In addition, there are tidal effects on the gravity potential due to the presence of external bodies. The gravitational field of celestial bodies generates, e.g., solid earth tides and ocean tides. Other tidal contributions are related to the Earth's rotation (length of day tide) and polar motion (solid earth pole tide and ocean pole tide) which are represented through degree-2 spherical harmonic coefficients (Voigt et al., 2016). A large scale, gravity potential variations also result from non-tidal mass redistributions in the atmosphere, ocean, and terrestrial water storage. The slow creeping motion of the mantle and the corresponding land uplift due to glacial isostatic adjustment (GIA) also contribute to the time-variable gravity signal. Here, these variations of Earth's gravity potential which are due to the non-tidal mass redistributions, are the signals that aim to be detected using clocks. Those time-variable changes in the gravitational potential δV between two clock sites can be represented through the differences of normalized Stokes coefficients $\delta \overline{C}_{nm}$ and $\delta \overline{S}_{nm}$ for a spherical harmonic degree n and order m with normalized associated Legendre function $\overline{P}_n^m(\cos\theta)$ (Hofmann-Wellenhof and Moritz, 2006):

$$\delta V(\lambda, \theta, r) = \frac{GM}{R} \sum_{n=0}^{\infty} \left(\frac{R}{r}\right)^{n+1} \sum_{m=0}^{n} \overline{P}_n^m(\cos\theta)$$
$$(\delta \overline{C}_{nm} \cos m\lambda + \delta \overline{S}_{nm} \sin m\lambda). \tag{1}$$

When loading or unloading takes place, the mass redistributions cause gravity potential variations (direct effect) as well as either an elastic or the viscoelastic response of the surface (indirect effect). The time-independent elastic response in terms of displacement and potential perturbation by the surface loads is described by Farrell (1972) using the Love number spectrum. To account for the relaxation process that accompanies deglaciation, a time-dependent impulse response function, obtained by convolution of the Heaviside Green function with the time dependent Love numbers, have to be considered as given by Peltier (1974):

$$h_n'(t) = h_n^{v'}(t) + h_n^{e'}\delta(t), \tag{2}$$
$$k_n'(t) = k_n^{v'}(t) + k_n^{e'}\delta(t). \tag{3}$$

$h_n'(t)$ and $k_n'(t)$ represent the time-dependent load Love numbers defining the vertical displacement and potential perturbation, respectively. Equations (2) and (3) consist of an instantaneous elastic response (v) plus a long-term viscous behavior (e) which indicates a elasticoviscous transition. Thus the total response function for the viscoelastic problem requires Green functions with time as well as space-dependent elements.

The global gravity field models that are derived from satellite geodesy only account for the direct effects of potential perturbations δV, as this is the effect for a fixed point in space. On the deformable Earth's surface, the potential variations due to the vertical displacement also have to be accounted for defining the total potential variation (Voigt et al., 2016). Thus, the effective potential variation associated with a loading potential V_n' as given by Schröder et al. (2021) at a terrestrial clock site is

$$\delta U = \sum_n \left(1 + k_n'(t) - h_n'(t)\right)V_n' = \delta V - g\delta h \tag{4}$$

where $\delta V = \sum_n \left(1 + k_n'(t)\right)V_n'$ is what one can obtain from satellite based measurements, $g\delta h = \sum_n h_n'(t)V_n'$, the potential variation due to geometrical distortion is given as vertical deformation δh from GNSS like measurements. As the potential change due to vertical deformation is also included in our clock simulations, the error should be beyond the clock's measurement accuracy, which is given by high precision GNSS (Schröder et al., 2021). The uncertainties in GNSS monthly data is in the order of a few millimeters which is beyond recent clock uncertainties.

3. Gravitational redshift and atomic clocks

The geometry of space–time is related to the distribution of matter as given by Einstein's field equation (EFE). The space–time curvature or the motion of a freely falling body is defined by the metric tensor $(g_{\alpha\beta})$, which can be obtained by solving the EFE (Hartle, 2021). According to general relativity theory, a clock ticks faster when kept far from a massive body compared to one near to it due to the difference in gravitational potential at the two locations. To derive these effects, relativistic reference frames like BCRS (Barycentric Celestial Reference System) and GCRS (Geocentric Celestial Reference System) are established (Müller et al., 2008). Each clock measures its own proper time interval $d\tau$ that is related to the relativistic line element ds

$$ds^2 = g_{\alpha\beta}(x^\gamma)dx^\alpha dx^\beta = -c^2 d\tau^2. \tag{5}$$

$x^\gamma = (x^0, x^1, x^2, x^3)$ represents the space–time coordinates with $x^0 = ct$ where t is the coordinate time and c is the velocity of light. When using the GCRS metric up to the

first Newtonian order (orders of c^{-4} are omitted), the fundamental time equation reads

$$\frac{d\tau}{dt} = 1 - \frac{1}{c^2}\left(V + \frac{v^2}{2}\right) + O(c^{-4}), \qquad (6)$$

where v is the coordinate velocity with respect to GCRS and V is the gravitational potential at the clock location (Denker et al., 2018). It comprises the effects of Earth's gravitational field and tidal effects due to external bodies (Sun, Moon, planets). On the Earth surface, the velocity is caused by the Earth's rotation. Therefore, the velocity term in Eq. (6) can be expressed as centrifugal potential Φ, which together with the gravitational potential, gives the gravity potential W.

The gravitational redshift is defined as the increase in the wavelength of the electromagnetic signal under the influence of a gravitational potential. Hence, the time dilation caused by the gravity potential difference at the two earth bound clocks can be identified in terms of the frequency shift between the clocks. When the clock observations are made simultaneously in the Earth-fixed system, the coordinate time interval of both clocks is the same, $dt_A = dt_B$. The ratio of the proper time at the two locations A and B with respect to time-dependent gravity potentials W_A and W_B is

$$\frac{d\tau_B}{d\tau_A} = \frac{f_A}{f_B} = \frac{1 - W_B/c^2}{1 - W_A/c^2}. \qquad (7)$$

Thus, the fractional frequency change between the two clocks is given as (Müller et al., 2018; Denker et al., 2018)

$$\frac{\Delta f}{f_A} = \frac{f_B - f_A}{f_B} = \frac{W_B - W_A}{c^2} \approx \frac{\delta U_B}{c^2}. \qquad (8)$$

In the following, we assume that one clock, e.g. A, is the reference clock at a stable location (without time-variable changes). The static part of the centrifugal effect cancels and its variations are assumed to be less than the systematic clock uncertainty, hence, $W_B - W_A$ can be approximated by δU_B in Eq. (8). Thus, via the observation of the frequency change with respect to a clock at a stable location A, the accurate detection of temporal variations of the Earth's gravity field at any clock site B is possible.

Clock performances are often characterized by their fractional uncertainty and instabilities (Sharma et al., 2020). The fractional frequency uncertainty determines the sensitivity of the shift detection. It has significant relevance in geodesy. McGrew et al. (2018) discuss ytterbium optical lattice clocks with a systematic uncertainty of 1.4×10^{-18}. A systematic uncertainty of 2×10^{-18} for SrI optical lattice clocks can be achieved by effectively controlling the atom environment (Bothwell et al., 2019). Takamoto et al. (2022) developed transportable Sr optical lattice clocks to operate with an uncertainty of 4×10^{-18}. The systematic uncertainty of the optical fiber link is of 10^{-19} when operated in a loop configuration (Lisdat et al., 2016) which is below the measurement accuracy of

optical clocks. Detection of time-dependent gravity potential variations requires high performance clocks with a fractional frequency uncertainty of 10^{-18} or better.

4. Methodology of simulation

The purpose of this simulation study is to prove that networks of high performance clocks can supplement the traditional geodetic techniques in determining mass variations on Earth. To quantify the effective potential variations δU (see Eq. (4)) resulting from different mass redistribution processes, four regions with different dominating dynamics - Himalaya, Amazon, Greenland, and Fennoscandia - are considered. The potential variations associated with each temporal change process are simulated as they can be observed by clocks. As terrestrial clocks measure the effective potential variation on a deformable Earth, we require to model the clock observations by combining GRACE and GNSS data (Eq. (4)). We modeled the temporal potential variations due to mass changes at assumed clock sites using the GRACE monthly solutions, and the corresponding surface deformations using GNSS time series of vertical displacements.

The clock sites are assumed at selected GNSS stations from the Nevada Geodetic Laboratory (NGL) network. The stations are chosen based on the data availability to have long timeseries. We used ITSG-2018 GRACE monthly solutions containing the full hydrological, cryospheric, and GIA signals, whereas mass variation in the oceans and atmosphere is reduced in the standard processing (Kvas et al., 2019). The time-variable gravity signals on a monthly basis are estimated as differences to the static gravity field model EIGEN-6C4 which is a mean over a long time period (Förste et al., 2014). The potential variations due to surface deformation are determined by taking monthly averages of daily solutions of vertical displacements from GNSS. The up components of NGL daily time series (Blewitt et al., 2018) solutions are given in the IGS14 (International GNSS Service) reference system which is closely related to ITRF2014. Non-tidal loading effects such as atmospheric loading, ocean bottom pressure, and surface hydrology are not removed in these solutions, yet. The dominant effect for displacements is due to non-tidal atmospheric loading (ATML) which is reduced from the GNSS data to be consistent with the GRACE seasonal signals in test cases I and II. Daily averages of the 3 hourly ATML data from GFZ in the center of figure frame (CF) solutions (Dill and Dobslaw, 2013) are computed and subtracted from the GNSS time series to only consider the time-variable signals of interest. Thus, the seasonal signals due to the terrestrial water storage variations (Himalaya and Amazon), and linear trends representing either the present-day ice mass variations (Greenland) or the GIA signals (Fennoscandia) were simulated as potential clock observations δU $\left(\approx \frac{\Delta f}{f} c^2\right)$. A 10^{-18} clock would be sensitive to potential variation of 0.1 m^2/s^2.

5. Results and discussions

5.1. Test case I - Himalaya

The Himalayan region with a glacier coverage of 33000 km^2 holds one-fifth of the Earth's total freshwater storage thus, also named as the 'Water tower of Asia'. Eastern Himalaya is wetter than Western Himalaya. The GNSS stations distributed over the Eastern Himalayas are now assumed as specific sites for clock observations (Fig. 1). Most of these stations lie on the Ganges-Brahmaputra–Meghna (GBM) river basin, which is one of the largest river systems in the world and hence, mostly affected by the terrestrial water storage variations. Here, seasonal hydrological signals with annual variations are simulated

by combining the detrended GRACE and GNSS datasets (Eq. (4)) as described in Section 4. These combined seasonal potential variations are fitted to annual cycles to better show what the signal looks like that can be observed by clocks. A total of 15 clock sites, 8 high-altitude stations, and 7 low-altitude stations, are considered.

Seasonal variations with a maximum range of $[-0.2 \quad 0.2]$ m^2/s^2 were obtained for the Himalayan region which can be detected using clock networks with a performance of 10^{-18} (0.1 m^2/s^2). The simulated clock observations in terms of effective potential variations for one high-altitude station (SMKT) and one low-altitude station (DNGD) are shown in Fig. 2.

The peak is in August for each station irrespective of the altitude or location, as the monsoon peaks in August. The
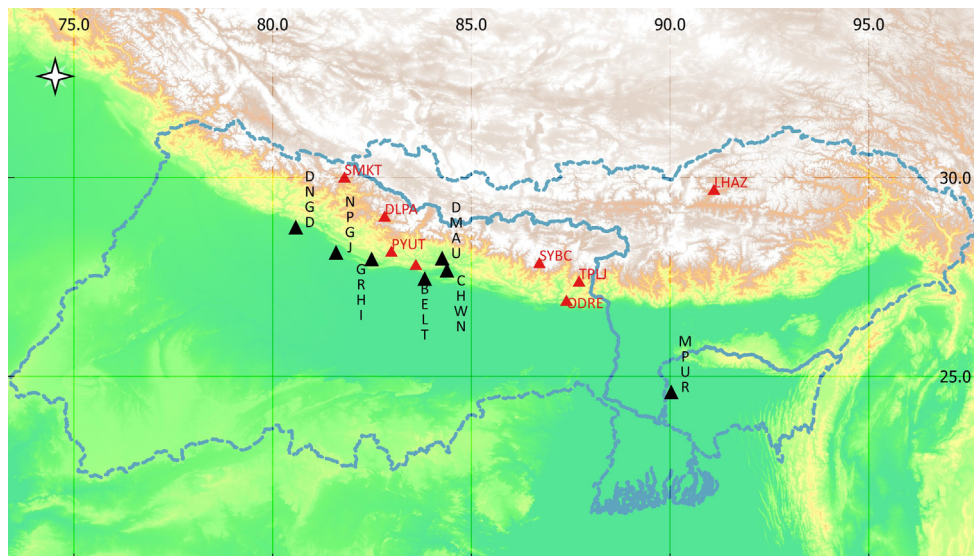

Fig. 1. Himalayan region with Ganges-Brahmaputra–Meghna river basin and assumed clock sites (high-altitude stations (red) low-altitude stations (black)).

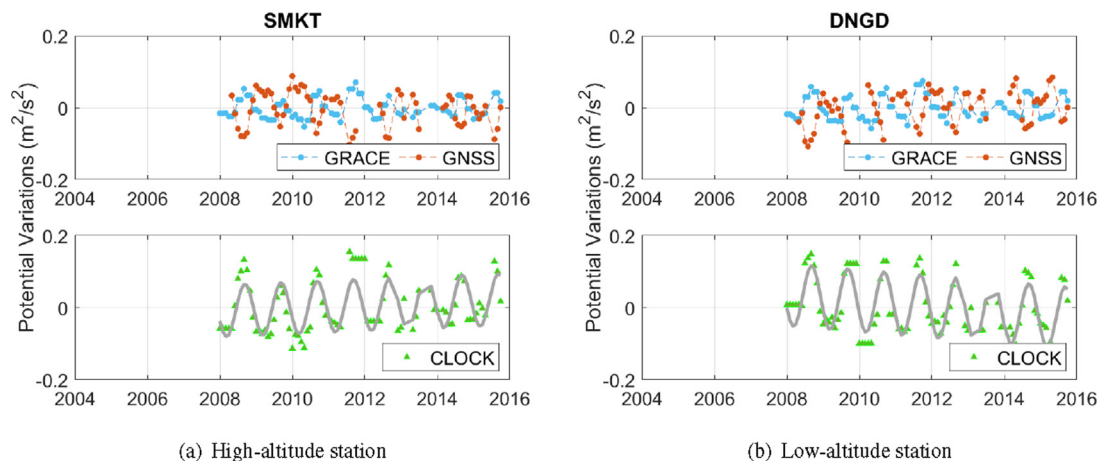

(a) High-altitude station

(b) Low-altitude station

Fig. 2. Simulated potential variations of the hydrological signal at Himalayan sites SMKT and DNGD. The upper panels show the variations separately derived from GRACE and GNSS. The lower panels show the combined effect of height change (GNSS) and mass change (GRACE) as it could be observed by clocks.

Table 1
Annual phase and amplitude of seasonal signal at clock sites at Eastern (LHAZ) and Western (NPGJ) Himalaya.

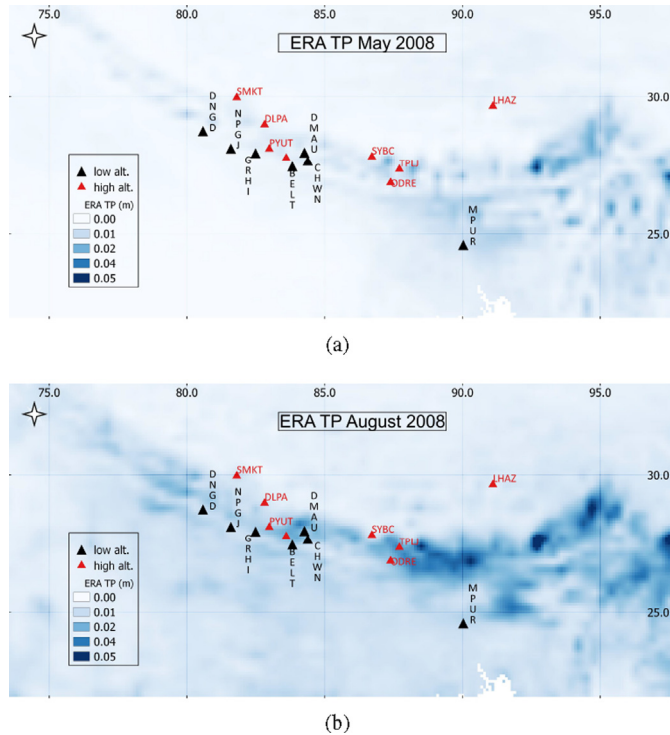| Station	Annual phase (deg)	Amplitude (m^2/s^2)
NPGJ	97.26	0.099
LHAZ	128.07	0.106

(a)

(b)

Fig. 3. ERA-5 monthly total precipitation grids in the Himalayan region for the months May (a) and August (b) in 2008.

phases and amplitudes analysis of the annually fitted curves are given in Table 1 for the clock sites NPGJ and LHAZ. The early and long-lasting precipitation patterns in North-East India and its gradual spreading towards the West could be observed with time series of clock measurements in the future. The ERA-5 ECMWF monthly total precipitation reanalysis product for an early period (May) and peak period (August) of the monsoon shows the strength and spreading of the monsoon at various clock sites (Fig. 3).

5.2. Test case II - Amazon

The largest river basin on Earth, the Amazon, is also home to Earth's largest rainforest. Here, we simulate the seasonal terrestrial water storage (TWS) changes as they could be observed by clocks. Based on the availability of long time series, four stations have been considered for the study (Fig. 4). Again we use Eq. (4) for modeling the clock observations.

TWS change in the Amazon region shows an annual peak to peak range of $[-0.5 \quad 0.5]$ m^2/s^2. Fig. 5 illustrates the simulated signals at the four stations BOAV, NAUS, BELE, and POVE as they can be observed by clocks. Amazon's seasonal properties of annual rainfall variability at the north and south of the equator are clearly visible from the variations in the phase values given in Table 2. The rainy season in the North of the equator is during summer from June to August, but from November to April in the South of the equator (Fig. 6) (Lindsey, 2007). The seasonal properties are associated with the direction of trade winds. In the north site, BOAV, the peak occurs in July and it is in April for the site in the south. Hence, those regional properties of the Amazon can be monitored by clock networks in the future.
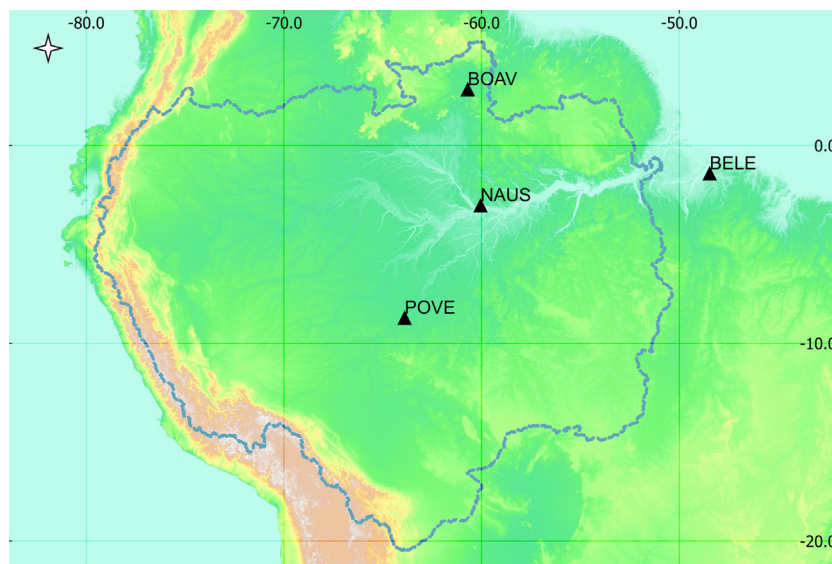

Fig. 4. Simulated clock sites in the Amazon basin.
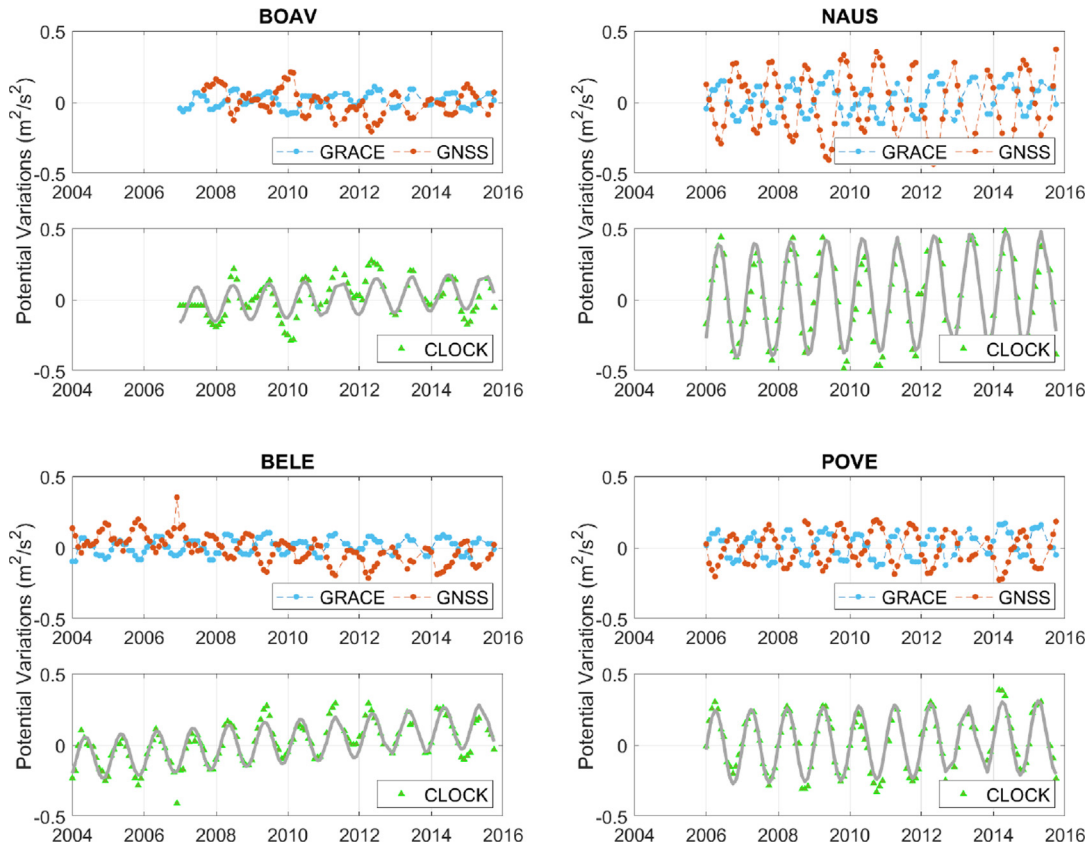
A. Vincent, J. Müller

Fig. 5. Simulated potential variations of hydrological signals at Amazonian sites BOAV, NAUS, BELE, and POVE. The upper panels show the variations separately derived from GRACE and GNSS. The lower panels show the combined effect of height change (GNSS) and mass change (GRACE) as it could be observed by clocks.

Table 2
Annual phase and amplitude of seasonal signals at clock sites in Amazonia.

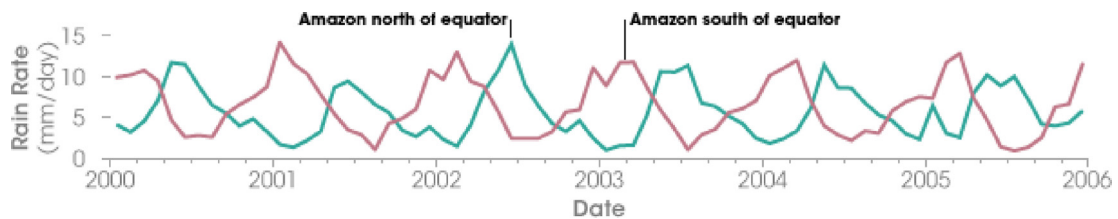| Station	Annual phase (deg)	Amplitude (m^2/s^2)	Month of maximum peak
NAUS	−129.37	0.406	May
POVE	−92.96	0.261	April
BOAV	−169.54	0.126	July
BELE	−129.34	0.153	May

Fig. 6. Rainfall variability in the north and south of the equator in the Amazon region. Image taken from NASA Earth Observatory (Lindsey, 2007).

5.3. Test case III - Greenland

The Greenland ice sheet is the world's second largest after Antarctica. Surface melting and iceberg calving due to climate change over several years have resulted in continuous ice mass loss mainly along the island's boundaries. This linear trend in the effective potential variation δU has

been simulated as to be observed by clocks. Here again, we followed the same simulation strategy as in the previous test cases. GNSS sites at four distant locations were considered for a better understanding of the rapid ice melt and the resulting elastic land uplift (Fig. 7). According to Landerer (2022) the overall ice mass loss estimated from GRACE and GRACE-FO during the period from 2002
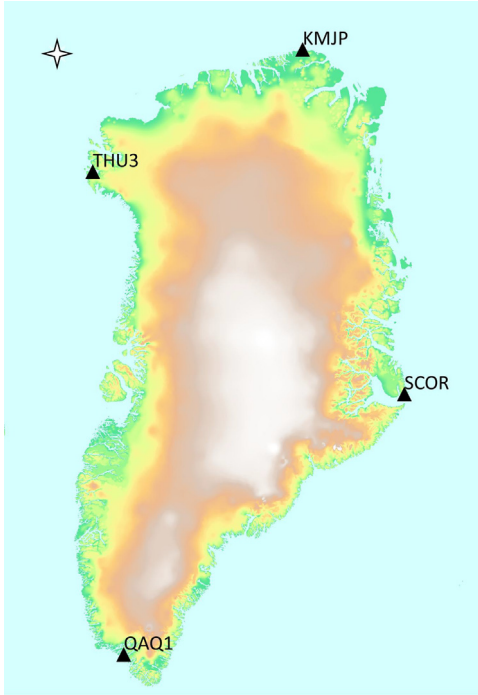
Fig. 7. Simulated clock sites considered in Greenland.

The simulated linear potential variations at the four GNSS locations KMJP, SCOR, THU3, and QAQ1 are shown in Fig. 8. The long term trend of the ice mass loss in Greenland between 2004 and 2015 causes signals of effective potential variations of 1 m^2/s^2 that again can clearly be observed by clock measurements. Additionally, the higher rates of potential mass variations in the west and south parts of Greenland can well be observed when clocks were run over the whole period. The linear potential variation is maximum at the THU3 site with a trend value of 0.11 m^2/s^2 per year.

5.4. Test case IV - Fennoscandia

The last ice age and the corresponding deglaciation which was completed about 10,000 years ago is the reason for the present-day GIA signals at previously ice covered areas (Olsson et al., 2019). An important observable of GIA is the secular gravity change and the associated land uplift, which is the viscoelastic response of the Earth as a result of the mantle creep. The central region possesses an uplift of 1 cm/yr or a corresponding secular gravity change of −20 nm/s^2 according to Ekman (1996).

The linear potential variations associated with the dominating GIA signal are simulated at 16 possible clock sites in Fennoscandia. The clock observations are simulated following the same methodology as discussed in the previous
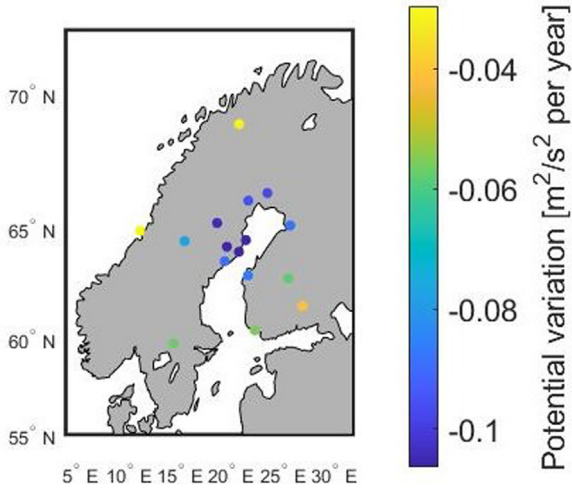
to 2020 is approximately 280 gigatons per year which results in 0.8 mm global sea level rise per year.

Fig. 8. Linear potential variations over Greenland at sites KMJP, SCOR, THU3, and QAQ1. The upper panels show the variations separately derived from GRACE and GNSS. The lower panels show the combined effect of height change (GNSS) and mass change (GRACE) as it could be observed by clocks.

Fig. 9. Simulated GIA signal over Fennoscandia in terms of effective potential variation per year.

It should be noted that the effective potential variations are dominated by the vertical uplift at the clock sites, the potential variations due to mass change only have a minor effect. Thus, clock networks may not add further information than GNSS in Fennoscandia. The geoid change due to GIA in the Fennoscandian uplift center is in the order of 0.4 mm per year, as given by the ICE6G-D model (Peltier et al., 2018), which can not be measured by clocks with fractional frequency uncertainty of 10^{-18}.

6. Conclusions and future research

In the future, clock observations can be used for observing potential variations due to mass changes and vertical deformation at the sites. Four case studies illustrate impressively that terrestrial clock networks can be applied as a modern and complementary tool for detecting various time-variable signals due to different mass re-distribution processes. As the investigated time-dependent effective potential variations are in the order of 0.1 m^2/s^2 up to 1 m^2/s^2, high performance clocks with a fractional frequency uncertainty of 10^{-18} (0.1 m^2/s^2) can measure these signals significantly. Relativistic geodesy can provide point-wise potential changes within short time (hours to days). Additionally, gravity variations obtained from satellite geodesy techniques can be validated.
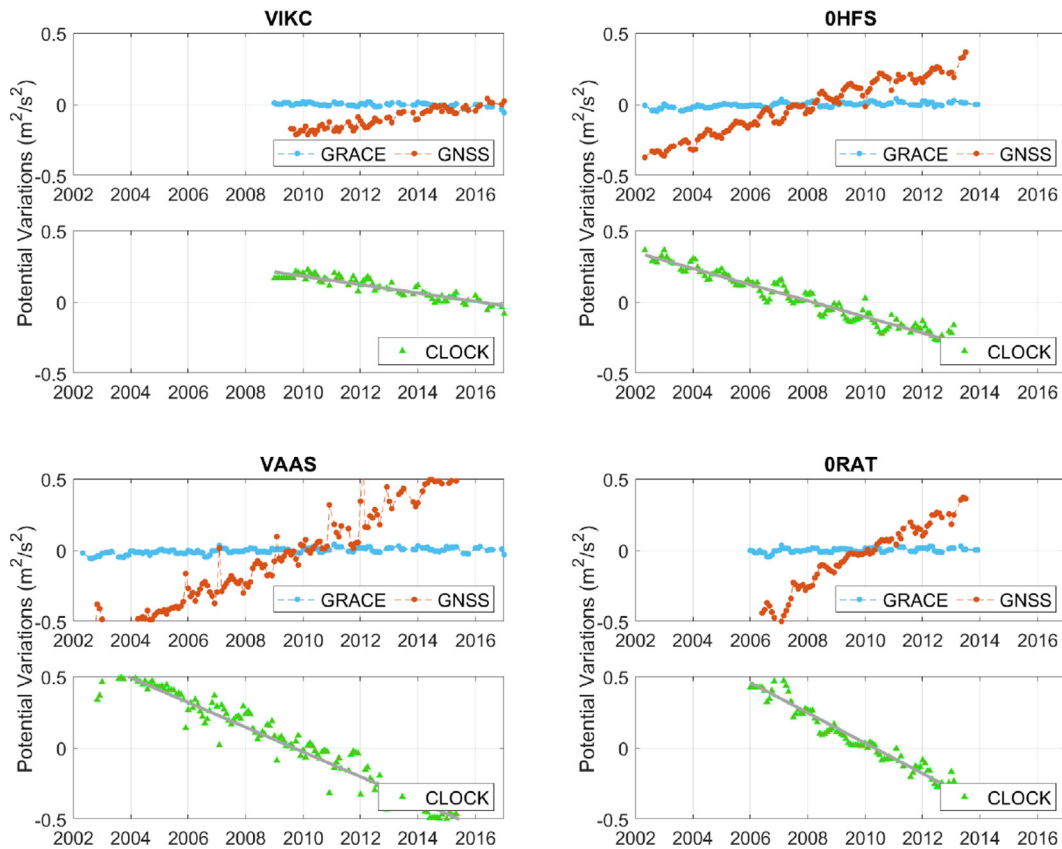
test cases. The sites near the uplift center experience an effective potential variation of 0.11 m^2/s^2 per year which decreases with distance from the central region (Fig. 9). The simulated clock observations of the GIA signal for a timespan from 2002 to 2016 at four locations with different trend values are given in Fig. 10.

Fig. 10. Linear potential variations in Fennoscandia at sites VIKC, VAAS, 0RAT, and 0HFS dominated by the vertical deformation. The upper panels show the variations separately derived from GRACE and GNSS. The lower panels show the combined effect of height change (GNSS) and mass change (GRACE) as it could be observed by clocks.

Different time-variable signals like the hydrologically driven annual variations (Himalaya and Amazon), the linear trend due to present-day ice mass loss (Greenland), and post glacial rebounding (Fennoscandia) were simulated as effective potential variations based on GRACE and GNSS data. The reference clock for clock comparison was supposed to be at a stable location on the ground or in a known satellite orbit. Optical links were assumed to be provided with sufficient uncertainties, i.e., better than 10^{-19}. Considering the quick development in the performance of atomic clocks, relativistic geodesy may enable novel Earth system observations that complement the existing geodetic techniques in the near future.

Declaration of Competing Interest

The authors declare that they have no known competing financial interests or personal relationships that could have appeared to influence the work reported in this paper.

Acknowledgments

References

Bjerhammar, A., 1985. On a relativistic geodesy. Bulletin géodésique 59 (3), 207–220. https://doi.org/10.1007/BF02520327.

Bjerhammar, A., 1986. Relativistic geodesy. Rockville, MD: U.S. Dept. of Commerce, National Oceanic and Atmospheric Administration, National Ocean Service, Charting and Geodetic Services, For sale by the National Geodetic Information Center, NOAA.

Blewitt, G., Hammond, W.C., Kreemer, C., 2018. Harnessing the gps data explosion for interdisciplinary science. Eos 99, 485. https://doi.org/10.1029/2018EO104623.

Bothwell, T., Kedar, D., Oelker, E., et al., 2019. JJila sri optical lattice clock with uncertainty of 2.010-18. Metrologia 56 (6), 065004. https://doi.org/10.1088/1681-7575/ab4089.

Delva, P., Denker, H., Lion, G., 2019. Chronometric geodesy: Methods and applications. In: Puetzfeld, D., Lämmerzahl, C. (Eds.), Relativistic Geodesy: Foundations and Applications. Springer International Publishing, Cham, pp. 25–85. https://doi.org/10.1007/978-3-030-11500-5_2.

Denker, H., Timmen, L., Voigt, C., et al., 2018. Geodetic methods to determine the relativistic redshift at the level of 10^{-18} in the context of international timescales: a review and practical results. J. Geodesy. 92 (5), 487–516. https://doi.org/10.1007/s00190-017-1075-1.

Dill, R., Dobslaw, H., 2013. Numerical simulations of global-scale high-resolution hydrological crustal deformations. J. Geophys. Res.: Solid Earth 118 (9), 5008–5017. https://doi.org/10.1002/jgrb.50353.

Ekman, M., 1996. A consistent map of the postglacial uplift of fennoscandia. Terra Nova 8 (2), 158–165. https://doi.org/10.1111/j.1365-3121.1996.tb00739.x.

Farrell, W., 1972. Deformation of the earth by surface loads. Rev. Geophys. 10 (3), 761–797. https://doi.org/10.1029/RG010i003p00761.

Förste, C., Bruinsma, S.L., Abrikosov, O., et al., 2014. Eigen-6c4 the latest combined global gravity field model including goce data up to degree and order 2190 of gfz potsdam and grgs toulouse. GFZ Data Services. 10. https://doi.org/10.5880/icgem.2015.1.

Hartle, J., 2021. Gravity: An Introduction to Einstein's General Relativity. Cambridge University Press, Cambridge. https://doi.org/10.1017/9781009042604.

Hofmann-Wellenhof, B., Moritz, H., 2006. Physical Geodesy. Springer Science & Business Media, Vienna. https://doi.org/10.1007/b139113.

Kvas, A., Behzadpour, S., Ellmer, M., et al., 2019. Itsg-grace2018: Overview and evaluation of a new grace-only gravity field time series. J. Geophys. Res.: Solid Earth 124 (8), 9332–9344. https://doi.org/10.1029/2019JB017415.

Landerer, F.W., 2022. Hyperwall: Greenland ice mass loss 2002–2021 - nasa. URL: https://svs.gsfc.nasa.gov/31156.

Lindsey, R., 2007. The amazon's seasonal secret. URL: https://earthobservatory.nasa.gov/features/AmazonLAI/amazon_lai.php.

Lisdat, C., Grosche, G., Quintin, N., et al., 2016. A clock network for geodesy and fundamental science. Nat. Commun. 7 (1), 1–7. https://doi.org/10.1038/ncomms12443.

Love, A.E.H., 1909. The yielding of the earth to disturbing forces. Proc. Roy. Soc. London. Series A, Contain. Papers Mathe. Phys. Character, 82(551), 73–88. https://doi.org/10.1098/rspa.1909.0008.

McGrew, W., Zhang, X., Fasano, R., et al., 2018. Atomic clock performance enabling geodesy below the centimetre level. Nature 564 (7734), 87–90. https://doi.org/10.1038/s41586-018-0738-2.

Müller, J., Dirkx, D., Kopeikin, S.M., et al., 2018. High performance clocks and gravity field determination. Space Sci. Rev. 214 (1), 1–31. https://doi.org/10.1007/s11214-017-0431-z.

Müller, J., Soffel, M., Klioner, S.A., 2008. Geodesy and relativity. J. Geodesy. 82 (3), 133–145. https://doi.org/10.1007/s00190-007-0168-7.

Olsson, P.-A., Breili, K., Ophaug, V., et al., 2019. Postglacial gravity change in fennoscandia—three decades of repeated absolute gravity observations. Geophys. J. Int. 217 (2), 1141–1156. https://doi.org/10.1093/gji/ggz054.

Pail, R., Bingham, R., Braitenberg, C., et al., 2015. Science and user needs for observing global mass transport to understand global change and to benefit society. Surv. Geophys. 36 (6), 743–772. https://doi.org/10.1007/s10712-015-9348-9.

Peltier, W., 1974. The impulse response of a maxwell earth. Rev. Geophys. 12 (4), 649–669. https://doi.org/10.1029/RG012i004p00649.

Peltier, W.R., Argus, D.F., Drummond, R., et al., 2018. Comment on an assessment of the ice-6g_c (vm5a) glacial isostatic adjustment model by purcell. J. Geophys. Res.: Solid Earth 123, 2019–2028. https://doi.org/10.1002/2016JB013844.

Schröder, S., Stellmer, S., Kusche, J., 2021. Potential and scientific requirements of optical clock networks for validating satellite-derived time-variable gravity data. Geophys. J. Int. 226 (2), 764–779. https://doi.org/10.1093/gji/ggab132.

Sharma, L., Rathore, H., Utreja, S., et al., 2020. Optical atomic clocks for redefining si units of time and frequency. MAPAN 35 (4), 531–545. https://doi.org/10.1007/s12647-020-00397-y.

Takamoto, M., Tanaka, Y., Katori, H., 2022. A perspective on the future of transportable optical lattice clocks. Appl. Phys. Lett. 120 (14), 140502. https://doi.org/10.1063/5.0087894.

Tapley, B.D., Watkins, M.M., Flechtner, F., et al., 2019. Contributions of grace to understanding climate change. Nat. Climate Change 9 (5), 358–369. https://doi.org/10.1038/s41558-019-0456-2.

Voigt, C., Denker, H., Timmen, L., 2016. Time-variable gravity potential components for optical clock comparisons and the definition of international time scales. Metrologia 53 (6), 1365. https://doi.org/10.1088/0026-1394/53/6/1365.

Wu, H., Müller, J., Lämmerzahl, C., 2019. Clock networks for height system unification: a simulation study. Geophys. J. Int. 216 (3), 1594–1607. https://doi.org/10.1093/gji/ggy508.